Volume 1 | Number 1 | Jan 2013 | Pages 1–100

PCCP

Physical Chemistry Chemical Physics
www.rsc.org/pccp

ROYAL SOCIETY OF CHEMISTRY

ROYAL SOCIETY OF CHEMISTRY

www.rsc.org/pccp

ARTICLE TYPE

Ultrafast Intersystem Crossing Dynamics in Uracil Unravelled by Ab Initio Molecular Dynamics†

Martin Richter, Sebastian Mai, Philipp Marquetand∗, and Leticia González

Ab initio molecular dynamics simulations have been performed in order to investigate the relaxation dynamics of uracil after UV excitation in gas phase. Intersystem crossing (ISC) has been included for the first time into time-dependent simulations of uracil, allowing the system to relax in the singlet as well as in the triplet states. The results show a qualitatively different picture than similar simulations that include singlet states only. The inclusion of ISC effectively quenches the relaxation to the singlet ground state and instead privileges transitions from the low-lying $n\pi^*$ state (S_1) to a $\pi\pi^*$ triplet state (T_2) followed by rapid internal conversion to the lowest triplet state.

1 Introduction

The interaction of ultraviolet (UV) light with deoxyribonucleic and ribonucleic acid (DNA/RNA) can lead to molecular photodamage and ultimately to mutations in the genetic code.[1] Despite this possibility, DNA and RNA, as well as their building blocks – the nucleobases – are remarkably photostable. This means that, after light irradiation the excited molecules activate photophysical mechanisms that efficiently return the system to the electronic ground state before detrimental excited-state reactions can take place. The quest to understand how these molecules transform the absorbed energy into heat, redistributing it as kinetic energy among all the degrees of freedom and dissipating it into the environment avoiding damage, has become a hot topic.[2–6] Accordingly, the last decade has witnessed a large number of experimental and theoretical studies on this subject.

Ultrafast time-resolved femtosecond (fs) spectroscopic studies[7–22] have shown that the relaxation of nucleobases is not a single molecular process but rather a complex one, consisting of several subprocesses, which take place on different time scales. Although the specifics depend on the experimental setup, usually one subprocess is found to correspond to a time constant on the order of fs accompanied by another one on the time scale of a few picoseconds (ps); in some cases, longer subprocesses on the order of nanoseconds (ns) can also be detected.

With the help of extended theoretical methods, it seems now well-established that the observed ultrafast time scales responsible for photostability are the result of decay due to internal conversion (IC) via conical intersections (CoIn), which are able to bring the excited molecule from the manifold of electronically excited singlet states to the ground state in a ps or sub-ps time scale.[23–26] Less clear, however, is the role played by intersystem crossing (ISC) in the photodeactivation of nucleobases.

Static quantum chemical computations have proposed that ISC from the singlet to the triplet manifold should be possible in some of the nucleobases.[27–33] The direct observation of triplet states is experimentally difficult if their quantum yield is small.[7,34,35] Moreover, the standard pump-probe setups employed[7,19–21] do not use a probe wavelength that can detect low-lying triplet states after excitation;[36] therefore, the presence of triplet states is in most cases inferred indirectly. This has not prevented, however, to correlate triplet states[15,16] to the long-lived transients observed experimentally. Despite the fact that spin-orbit couplings (SOC) are small in organic molecules and thus ISC is traditionally conceived as a slow process in comparison to IC,[37] recently our group has demonstrated that, in cytosine, ISC can take place on an ultrafast time scale of few hundreds of fs, hence also contributing to the fs and ps time constants detected experimentally.[26,36,38] While ISC is astonishingly fast in this case, cytosine seems to be not the only organic molecule where ISC and IC processes can compete on the same time scale. Experimental fast to ultrafast times scales for ISC have been reported for aldehydes,[39] a number of small aromatic compounds, such as benzene,[40,41] naphthalene, anthracene and their carbonylic derivatives[42–55] as well as nitrocompounds[46,56–68]. The substitution of oxygen by sulfur in nucleobases enhances ISC so dramatically that the ultrafast IC responsible for photostability disappears

while turning ISC to the lowest triplet states into the most efficient deactivation pathway – with enormous consequences for photodamage.[64–66,69–74] The dimerization of pyrimidine nucleobases, one of the most abundant lesions in UV-irradiated DNA, is also claimed to be mediated by triplet states.[35,75,76]

ISC is clearly an important photophysical process; however, dynamical simulations accounting for spin transitions are very much underrepresented in comparison to studies dealing with IC. Spin-induced transitions have been simulated by wave packet propagations along one or few dimensions by Daniel and coworkers in organometallic compounds.[77–87] Several approaches, from quantum dynamics in reduced dimensions to semiclassical dynamics, have been combined to model and control the ultrafast spin-flip in dihalogens in argon matrices.[88–91] Surface-hopping methods have been also employed to study ISC in the S + H$_2$ reaction.[92] However, the modelling of dynamical processes including both IC and ISC on the same footing is much more recent, especially in full dimensions. The dynamics of coupled singlet and triplet states have been simulated with a reduced vibronic Hamiltonian for benzene,[41], HF[93] and with exact three-dimensional wave packets[94] as well as with ab initio molecular dynamics[95] for SO$_2$. Further semiclassical surface-hopping approaches using semiempirical Hamiltonians have been employed for acetone[96], pentanal[55] and 6-thioguanine[70], using time-dependent density functional theory for a few transition metal complexes[97,98] and using on-the-fly ab initio multiconfigurational calculations for the DNA nucleobase cytosine.[36,38]

In this work, we focus on uracil, an RNA nucleobase. Time-resolved experiments in uracil have been first reported by Kang _et al._[16] and later on by others.[12,13,15] Depending on the resolution, one, two, or three time constants have been resolved. The most recent experiments of Kotur et al.[12] and Matsika et al.[13] combine time-of-flight mass spectroscopy (TOF-MS) with strong field dissociative ionization, thereby yielding a picture of multiple bifurcations in the deactivation mechanism of uracil. There have been a number of dynamical simulations published dealing with uracil,[24,99–105] but none includes triplet states. Hence, the present study is designed to fill this gap, showing for the first time dynamics simulations including simultaneously non-adiabatic couplings (which mediate IC via CoIn) and SOC (which allows for ISC). We demonstrate that ISC competes with IC and should be taken into account to explain the ultrafast deactivation of uracil after UV irradiation. Further, the simulations presented in this paper aim at completing the knowledge on the fundamental question of which factors on the atomistic level contribute to the photostability of DNA/RNA, ultimately motivating experiments that can time-resolve non-adiabatic dynamics involving triplet states using emerging ultrafast photon technologies.

2 Methods

The molecular dynamics simulations on uracil has been carried out using the semiclassical ab initio molecular code SHARC,[106] which is a surface-hopping algorithm[107] able to deal with arbitrary couplings. Previous dynamical applications of SHARC can be found in Refs.[36,38,95,108–111]. This surface-hopping algorithm uses a fully diagonal, spin-mixed electronic basis, resulting from the diagonalization of the Hamiltonian containing non-adiabatic and spin-orbit couplings.[36,106] The integration of the nuclear motion is done with the Velocity-Verlet algorithm[112,113] with a time step of 0.5 fs for 1 ps; the time evolution of the quantum amplitudes is followed with a time step of 0.02 fs. Decoherence correction was taken into account using the energy-based method of Granucci and Persico with a parameter of $\alpha = 0.1$ hartree.[114]

The electronic energies, gradients, non-adiabatic couplings and SOCs were evaluated on-the-fly for each nuclear integration time step using the Complete Active Space Self-Consistent Field (CASSCF)[115,116] method and the 6-31G* basis set. Two different active spaces were employed: a (12,9) consisting of 12 electrons in 9 orbitals and a (14,10), with two electrons more in an additional orbital. The latter active space consist of 8 π/π^* orbitals as well as 2 n orbitals located at the oxygen atoms of uracil (see Figure 1), and it has been employed before for quantum chemical calculations[117] and molecular dynamics in the singlet manifold only.[104,105] The smaller active space contains one oxygen lone pair less. The excited state properties are calculated using the state-average CASSCF version, including the lowest four singlet states and the lowest three triplet states, i.e., 7 electronic states. Note that in the dynamics the triplet components were treated explicitly, giving 13 states in total. The assessment of the CASSCF energies has been done using single point calculations at the more accurate CASPT2[118,119] level of theory. All quantum mechanical calculations were performed using the MOLPRO 2012 package of programs.[120]
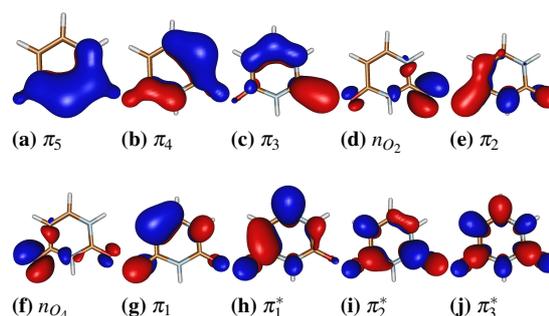
Fig. 1 Active space of uracil including 14 electrons in 10 orbitals. The (12,9) active space misses the n_{O_2} orbital.

(a) π_5 (b) π_4 (c) π_3 (d) n_{O_2} (e) π_2

(f) n_{O_4} (g) π_1 (h) π_1^* (i) π_2^* (j) π_3^*

For the generation of the initial conditions, the ground state equilibrium geometry was optimized at the CASSCF(14,10) or CASSCF(12,9) level of theory, as specified below. Using the corresponding harmonic frequencies, a Wigner distribution of 2000 uncorrelated velocities and geometries has been generated. For each initial condition a single point calculation has been performed to simulate an absorption spectrum from the oscillator strengths, as explained in Ref.[121]. The oscillator strengths also serve for selecting the number of trajectories to be propagated from each electronic excited state, assuming an instantaneous excitation (a δ-pulse).

The evaluation of trajectories is made only on those finishing the whole simulation time of 1 ps, unless specified otherwise, or residing in the S_0 or T_1 for at least 15 fs. For the statistical evaluation, we calculated so-called "spectroscopic" populations in addition to the ones in the molecular Coulomb Hamiltonian (MCH)[122] electronic basis. The transformation from the MCH basis to the spectrocopic one is done in an approximate manner using the transition dipole moment between the electronic ground and the calculated excited states. If the transition dipole moment is >0.05 a.u., the state is considered a bright $\pi\pi^*$ state and for values <0.05 a.u. the state is a dark $n\pi^*$ state. If the transition dipole moment is very small ($< 1 \cdot 10^{-6}$ a.u.) the state is assigned to a triplet state. The ground state S_0 corresponds always to the closed-shell state in the present case and therefore, we use the label S_0 also in the spectroscopic representation. Statistical analysis of the trajectory data within the spectroscopic representation provides a better description of the experimentally observed decay rates, since the physical properties of the spectroscopic states change less than in the MCH representation.[36]

3 Results and Discussion

3.1 Excitation Energies and Absorption Spectrum

The pyrimidine nucleobase uracil presents 13 different tautomers. Among them, this study focuses on the diketo form (Figure 2) since it is the biologically relevant and the dominant tautomer in gas phase and solution.[123]
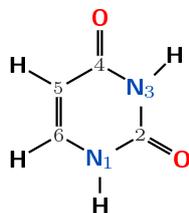

Fig. 2 Uracil in its diketo form, with ring atom numbering.

The experimental absorption spectrum of uracil shows its maximum at 244 nm (5.08 eV).[124] A number of excited state calculations for uracil are reported in the literature. Good surveys can be found in Refs.[23,125–127]. In Table 1, we compile excitation energies obtained at the CASSCF and CASPT2 levels of theory. Singlet and triplet states are given, as available. For all CASPT2 calculations, the band at ca 5.1 eV corresponds to the S_2 state, which is of $\pi\pi^*$ character and possesses the largest oscillator strength. The lowest-lying singlet state is of $n\pi^*$ character and its energy fits reasonably well within the energetic range recorded experimentally.[128] Taking as a reference the calculation of Climent *et al.*[29], who use CASPT2/CASSCF(14,10) and averaging separately singlet (SA4) and triplet (SA3) states, one can see that the nature of the S_3 state is more sensible to the level of theory. Using this SA4/SA3-CASPT2/CASSCF(14,10) protocol, the first excited dark $n\pi^*$ state is followed by two $\pi\pi^*$ states, whereas a SA7- calculation (where singlet and triplets states are averaged together) predicts a second $n\pi^*$ state as the S_3. The removal of one n-orbital (the n_{O_2}) from the active space (resulting in an (12,9) active space) yields the same order of states as in Climent *et al.*[29]. The use of symmetry to obtain the A' and A'' states separately, as done in the benchmark paper of Schreiber *et al.*[125], has a minor effect in the CASPT2 energies. The inclusion of dynamical correlation when going from CASSCF to CASPT2, in contrast, is more important, since it affects the singlet $\pi\pi^*$ states more dramatically than the $n\pi^*$ ones, thereby influencing greatly the energetic position of the singlet states in uracil. While S_1 and S_2 are almost degenerated at CASPT2, the destabilization of the $\pi\pi^*$ at CASSCF separates the states by more than 1 eV, making in turn the S_2 and S_3 very close in energy. The triplet states seem to be more robust with respect to the level of theory, both regarding the active space and the inclusion of dynamical correlation. The T_1 is a $\pi\pi^*$ state located at around 4 eV, well-separated energetically from an $n\pi^*$ and a second $\pi\pi^*$ state.

The critical analysis above illustrates that the choice of the level of theory for the dynamics can be very important, as the state energies are expected to influence the time evolution of the system and determine the population of the states. Particularly the energy gaps govern, together with the couplings, the hopping probabilities to other singlet states or to the triplet states, and therefore it seems natural to think that different levels of theory could deliver different results, distorting the interpretation of the experiments. Ideally, one would like to employ CASPT2 for the on-the-fly calculations since it is one of the most reliable ab initio methods in this case. Due to unfavorable scaling of CASPT2, we are limited to use CASSCF instead. Nevertheless, to assess the impact of the active space on the dynamics, the two active spaces ((14,10) and (12,9)) have been employed for the subsequent SHARC molecular dynamics calculations. The (14,10) active space has previously been used in the dynamical simulations of Fingerhut *et al.*[104,105] including singlets. The (12,9) active space is chosen since it

Table 1 Vertical excitation energies (in eV) of uracil at CASSCF and CASPT2 level of theory with different active spaces. State characters are also indicated and oscillator strengths are given in parentheses.

| State | experiments | CASPT2 | | | | CASSCF | | |
		SA4/SA3 (14,10)[a]	SA7 (14,10)	SA7 (12,9)	SA5/SA4 (10,8)/(14,10)[b]	SA4/SA3 (14,10)[a]	SA7 (14,10)	SA7 (12,9)
S_1	4.38[c]	$n\pi^*$ 4.93 (0.00)	$n\pi^*$ 4.91	$n\pi^*$ 4.85	$n\pi^*$ 4.90	$n\pi^*$ 5.18	$n\pi^*$ 5.13	$n\pi^*$ 4.83
S_2	5.1[d]	$\pi\pi^*$ 5.18 (0.20)	$\pi\pi^*$ 5.09	$\pi\pi^*$ 5.32	$\pi\pi^*$ 5.23	$\pi\pi^*$ 6.82	$\pi\pi^*$ 7.04	$\pi\pi^*$ 7.07
S_3	6.0[d]	$\pi\pi^*$ 6.18 (0.07)	$n\pi^*$ 6.41	$\pi\pi^*$ 6.02	$\pi\pi^*$ 6.15	$\pi\pi^*$ 7.29	$n\pi^*$ 7.07	$\pi\pi^*$ 7.33
T_1	—	$\pi\pi^*$ 3.80	$\pi\pi^*$ 3.90	$\pi\pi^*$ 3.90	—	$\pi\pi^*$ 3.98	$\pi\pi^*$ 4.00	$\pi\pi^*$ 3.93
T_2	—	$n\pi^*$ 4.71	$n\pi^*$ 4.84	$n\pi^*$ 4.71	—	$n\pi^*$ 4.87	$n\pi^*$ 4.95	$n\pi^*$ 4.65
T_3	—	$\pi\pi^*$ 5.33	$\pi\pi^*$ 5.54	$\pi\pi^*$ 5.47	—	$\pi\pi^*$ 5.76	$\pi\pi^*$ 5.86	$\pi\pi^*$ 5.70

[a] Ref. Climent *et al.* [29]
[b] For $\pi\pi^*$: SA5(A')-CASPT2(10,8)/6-31G*, For $n\pi^*$: SA4(A'')-CASPT2(14,10)/6-31G* from ref. Schreiber *et al.* [125]
[c] Ref. Masaaki Fujii and Ito [128]
[d] Ref. Clark *et al.* [124]

predicts the same order of the states as CASPT2. [29,125,129]

Using the 2000 uncorrelated geometries of the Wigner distribution, an absorption spectrum was calculated from the oscillator strengths and excitation energies. Figure 3 shows the absorption spectra calculated with both active spaces. As it can be seen, the system is initially excited to the S_2 and S_3 states. Both states are bright as a direct result of the distribution of the initial geometries around the equilibrium geometry. Even if the S_3 is a dark $n\pi^*$ at the ground state equilibrium geometry using the (14,10) active space, a small geometrical displacement can alter the order of state characters, especially when both states are energetically close. Thus, S_3 takes $\pi\pi^*$ character and hosts a significant amount of excited population. As a result, irrespective of the initial character of the states, both S_2 and S_3 contribute to the absorption spectrum obtained with CASSCF. The relative distribution of population in the S_2 and S_3 states depends, however, on the active space; specifically, the S_2 state dominates the spectrum in the energy region explored in our simulations with the (12,9) active space. Globally, the lack of dynamic correlation in the CASSCF method shifts this band towards higher excitation energies. Accordingly, the maximum of the simulated absorption spectrum is located at 176 nm (7.03 eV), overestimated by almost 2 eV, as in the papers of Nachtigallova *et al.* [103] using CASSCF(10,8) or Fingerhut *et al.* [104,105] using CASSCF(14,10).

Based on the obtained absorption spectra, four sets of trajectories were prepared (see Table 2). Ensemble I was taken as a reference set to assess the impact of ISC. Accordingly, only IC within the singlet states was allowed and any possible ISC towards the triplet states was neglected. This set contained 49 trajectories prepared at the CASSCF(14,10) level of theory, from which 26 and 23 were excited to the S_2 and S_3 states, respectively, according to the associated oscillator strengths. The trajectories were selected as to cover the full excitation range and were propagated during 600 fs. Ensemble II was composed of 120 trajectories from the CASSCF(14,10) initial conditions, also covering the full spectrum, and were split in
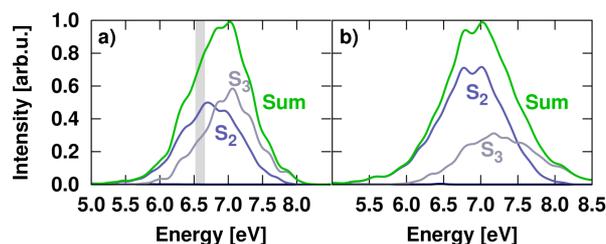
Fig. 3 Simulated absorption spectrum of uracil using SA7-CASSCF(14,10) (in panel a) and SA7-CASSCF(12,9) (in panel b) single point calculations. Grey area denotes the excitation energy window employed to model the experimental excitation energy in uracil.

64 and 56 over the states S_2 and S_3. Since experimental setups do not cover the full spectrum but use a laser pulse of fixed wavelength, a third set of trajectories (Ensemble III) was prepared to match the energy range accessed experimentally. Gas phase pump-probe experiments in uracil [12–14] typically employ a wavelength of 267 nm (4.64 eV) and pulse widths around 50 fs, resulting in an energy bandwidth of ± 0.07 eV. Accordingly, the experimental excitation wavelength is about 0.44 eV below the observed absorption maximum of 224 nm (5.08 eV). Hence, to investigate the influence of the excitation energy on the excited state dynamics of uracil, ensemble III was prepared from 64 trajectories, distributed as 37 and 27 in S_2 and S_3, respectively, resembling the distribution of states within the energy window of 0.14 eV centered around 6.59 eV. Finally, the influence of the active space is evaluated from the simulations of Ensemble IV, which comprises 40 trajectories, where CASSCF(12,9) was used in the dynamics instead of CASSCF(14,10). Energies were chosen to cover the full range of the theoretical absorption spectrum. From these trajectories, 28 and 12 were initially excited to the S_2 and S_3 states, respectively, and propagated for 500 fs.

Table 2 Ensembles of trajectories used in the dynamical simulations, with active space used, number of trajectories excited to S_2 and S_3, total number of trajectories propagated, number of states averaged in the CASSCF calculation, maximum propagation time and energy restrictions.

	Ensemble			
	I	II	III	IV
CASSCF	(14,10)	(14,10)	(14,10)	(12,9)
S_2 excitation	26	64	37	28
S_3 excitation	23	56	27	12
total	49	120	64	40
state averaging	SA4	SA7	SA7	SA7
t_{max} [fs]	600	1000	1000	500
restrictions	–	–	6.52-6.66 eV	–

3.2 Excited State Dynamics including Singlet States Only

A number of gas phase excited-state dynamical studies including only singlet states are available for uracil. In Figure 4 we have sketched the mechanisms derived from these studies.
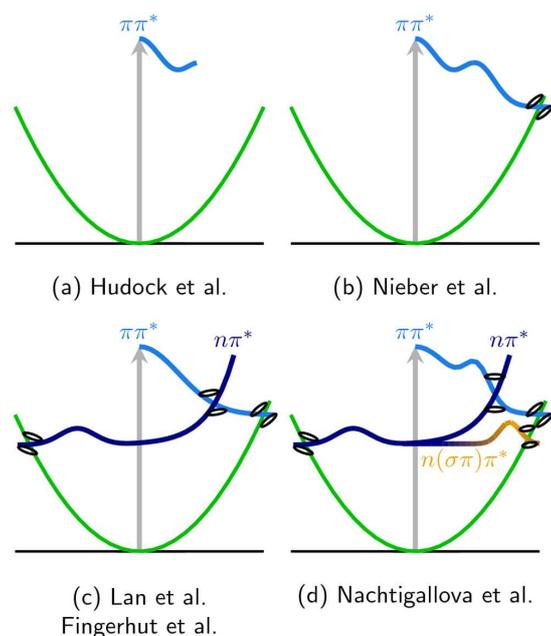
Fig. 4 Schematic overview of the proposed deactivation mechanisms of uracil, from Ref. [99] (**a**), Ref. [100] (**b**), Refs. [102,104,105] (**c**), and Ref. [103] (**d**). Note that the one-dimensional cartoons imply different reaction coordinates.

Using CASSCF(8,6) wavefunctions and full multiple spawning (FMS), Hudock et al. [99] found in 2007 that after excitation uracil gets trapped in the S_2 minimum (see Figure 4a). One year later, Nieber, Doltsinis and coworkers [100,101] em-

ployed surface-hopping trajectories coupled to Car-Parrinello dynamics on potentials calculated with the ROKS/BLYP approach and observed a sub-ps direct decay from the $\pi\pi^*$ state to the ground state, governed by the so-called ethylenic $\pi\pi^*/S_0$ CoIn (see Figure 4b and also section 3.4). The semiempirical-based OM2/MRCI simulations of Lan et al. [102] obtained two different relaxation mechanisms, as depicted in Figure 4c. The first path directly connects the bright $\pi\pi^*$ state with the S_0 ground state via the ethylenic CoIn, while the second, slower pathway, connects the initially excited $\pi\pi^*$ state with the $n\pi^*$ state via a planar S_2/S_1 CoIn that is located close to the Franck-Condon region. The trajectories spend some time in the $n\pi^*$ state until finally reaching the S_0 via a different S_1/S_0 CoIn.

The surface-hopping simulations at the CASSCF(10,8) level of theory of Barbatti et al. [24] and by Nachtigallova et al., [103] showed that three deactivation pathways (which involve three electronic states) are possible – see Figure 4d. The first one is equivalent to that suggested before in Refs. [99–101]: After initial trapping in the S_2 minimum, the trajectories go to the S_0 via a $\pi\pi^*/S_0$ CoIn. Interestingly, this path is not observed in a comparable study made on thymine, [130] even though thymine and uracil have very similar potential energy surfaces and analogous dynamics would be expected. The authors of Refs. [24,103] argue that the efficiency of the direct $\pi\pi^* \rightarrow S_0$ path in thymine is significantly reduced due to the heavy mass of the methyl group. The second pathway found in uracil is also not observed in thymine and involves a crossing with the $n\pi^*$ state. The implicated CoIn, termed ring-opening CoIn, leads to the destabilization of the ground state as the ring breaks. At these geometries the S_1 wavefunction contains contributions of σ orbitals and therefore it is described as a $\sigma(n-\pi)\pi^*$ state. In their work, it is also noted that this pathway would probably lead to photochemical products different from the equilibrium geometry. Interestingly, Buschhaus *et al.* [131] do observe ring opening after UV irradiation of nucleosides but the detected isocyanates (R–N=C=O) cannot arise directly from the N_3–C_4 bond cleavage predicted by Nachtigallova *et al.* [103]. The third deactivation pathway involves a change of character to $n\pi^*$ after initial trapping and relaxation through the S_2/S_1 CoIn. The trapping in the $n\pi^*$ minimum delays the ground state relaxation, affecting the time scales obtained.

The most recent surface-hopping simulations have been published by Fingerhut and coworkers [104,105] and are based on CASSCF(14,10) wavefunctions that describe four singlet states. After initial excitation a fast decay of the S_3 population is observed (not shown in Figure 4c), together with a slower decrease of S_2 population and an increase of S_1 population that exceeded the S_2 population after about 400 fs of simulation time, in agreement with the two mechanisms of Lan et al. [102] In the first pathway, the initially populated S_2 state of $\pi\pi^*$

character decays to the S_1 ($n\pi^*$) state, gaining more than 20% of population in less than 100 fs. In the $n\pi^*$ state, population can be trapped before decaying to the S_0, leading to long relaxation times. Interestingly, this study shows much less pronounced trapping in the S_2 state than the one of Nachtigallova et al. [103], even though both studies use CASSCF. Fingerhut et al. [104] attribute the difference to the size of the active space size. The second pathway involves a transition to S_1 without changing the state character (i.e. staying in the $\pi\pi^*$ state), followed by $\pi\pi^* \rightarrow S_0$ relaxation through the ethylenic CoIn. In their simulations, all trajectories that reached the ground state within 1 ps followed the second pathway and only a few trajectories relaxed via the first pathway in longer runs of up to 2 ps.
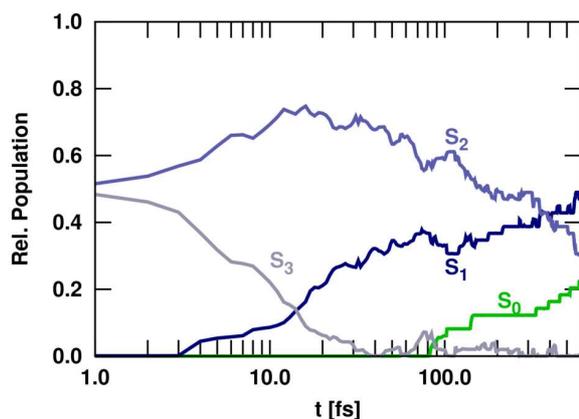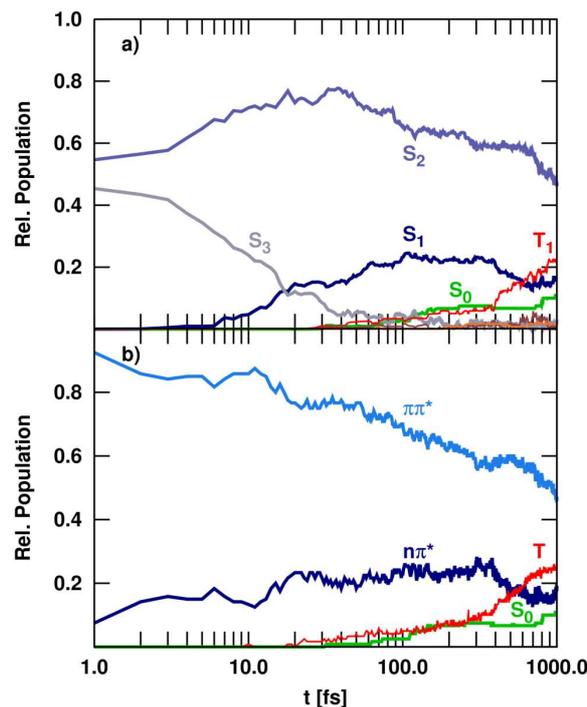

Fig. 5 Time evolution of the population of electronic states, including only singlet states (Ensemble I).

All the previous simulations can be compared with the results obtained using the Ensemble I of trajectories. Figure 5 shows the time evolution of the different state populations. Not surprisingly, our results are comparable to that of Fingerhut et al. [104] because they are made at a similar level of theory. In essence, the S_2 ($\pi\pi^*$) state decays to the S_1 ($n\pi^*$) and repopulation of the ground state occurs within 100 fs. As it will be shown in the next section, the inclusion of triplet states changes this picture dramatically.

3.3 Excited State Dynamics including Singlet and Triplet States

Figure 6a shows the time-evolution of the singlet and triplet state populations of the trajectories considered in the Ensemble II (recall Table 2). Although the propagations are made in the basis of fully diagonal, spin-mixed states, the analysis is carried out in the MCH and spectroscopic representations in order to be able to compare to previous studies.

As in the singlet-only case (Ensemble I), the trajectories ini-

Fig. 6 Time evolution of the population of electronic states, including singlet and triplet states (Ensemble II), in the MCH (a) and spectroscopic (b) representation.

tially excited to the S_3 state show a very efficient decay to S_2. Therefore, after 200 fs the S_3 is completely depopulated and after this time, this state plays a negligible role in the deactivation of uracil. This ultrafast IC from the S_3 generates substantial amount of population in the S_2 state, which within the first 40 fs collects about 75% of the total population – in similitude to the singlet-only case (Figure 5). During the rest of the propagation time, the population of the S_2 state decreases slowly due to IC to the S_1. However, after 1 ps still 50% of the excited trajectories are trapped in the S_2, indicating that the population resides in the surrounding of the S_2 minimum. The rest of the population is transferred to the S_1, which gains some population in the beginning from S_3 and later on slowly via $S_2 \rightarrow S_1$ transitions, but not as substantially as in Figure 5. From the S_1, some trajectories decay to the S_0 within the first 200 fs via the so-called ring opening CoIn (see Figure 10c in the next section). Only after this time, the S_0 population starts increasing very slowly, unlike in the singlet-only case. The reason is obviously that there is a significant amount of population accumulated in the triplet states after the total propagated time. With 22%, the T_1 state has the largest population, after the S_2 with 50%, whereas the S_1 accumulates up to 15% and other higher excited states (S_3, T_2, T_3) show only populations below 3%. The T_1 state is mostly populated via $S_1 \rightarrow T_2$ ISC,

followed by very efficient $T_2 \rightarrow T_1$ IC. This qualitative distribution of populations is fundamentally different from the case where only transitions within the singlet manifold is allowed (Ensemble I shown in Figure 5) because an additional channel (ISC) has been opened to compete dynamically with IC.

Neglecting the possibility of ISC in the simulations results in a strong increase of $n\pi^*/S_1$ population. Thus, the population of the singlet $n\pi^*$ state exceeds the population of the $\pi\pi^*/S_2$ state after about 400 fs (Figure 5). This population inversion is not observed in the simulations that allow for population of the triplet states via ISC (Figure 6a). Here, the depopulation of S_1 due to ISC processes prevents the population inversion of the excited singlet states as well as the efficient population of the S_0 ground state within 1 ps. Thus, our simulations suggest that ISC processes in uracil are too slow to compete with IC of the excited singlet states in the early times, but can significantly alter the fate of the population trapped in the lowest excited singlet state. As a result, IC to the ground state and ISC to the triplet manifold are in direct concurrence. A general decay scheme summarising the processes discussed above is given in Figure 7a.
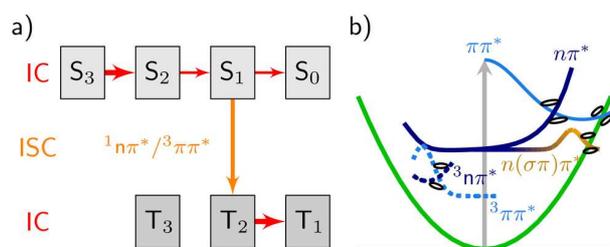

Fig. 7 Overview of the processes observed in uracil. a) MCH representation: The thickness of the arrows indicates the extent of population transfer. IC and ISC stand for internal conversion and intersystem crossing, respectively. b) Spectrocopic representation: Although one-dimensional, the plot implies multiple reaction coordinates.

The majority of the $S_1 \rightarrow T_2$ transitions follow El-Sayed's rule,[132,133] i.e. the transitions involve a change of state character in the singlet-triplet transition. Usually the S_1 is of $n\pi^*$ character and the T_2 is of $\pi\pi^*$ character (see electronic supplementary information (ESI)† on how to evaluate the state character), resulting in large SOCs that peak above 60 cm^{-1} (39 cm^{-1} on average). The energy difference of the involved states at the ISC geometries is very small, 0.01 eV (98 cm^{-1}) on average, favouring the process of ISC.[31]

Restricting the allowed excitation energy range to 6.59 ± 0.07 eV (Ensemble III) yields qualitatively similar results, see Figure 8. However, the energetic restriction leads to a smaller triplet yield and a concomitant slightly larger population in the ground state. This behaviour results from the smaller total energy of the trajectories which reduces the probability to reach

geometries that allow for efficient ISC, giving the system more time to relax via S_1/S_0 CoIns to the electronic ground state.
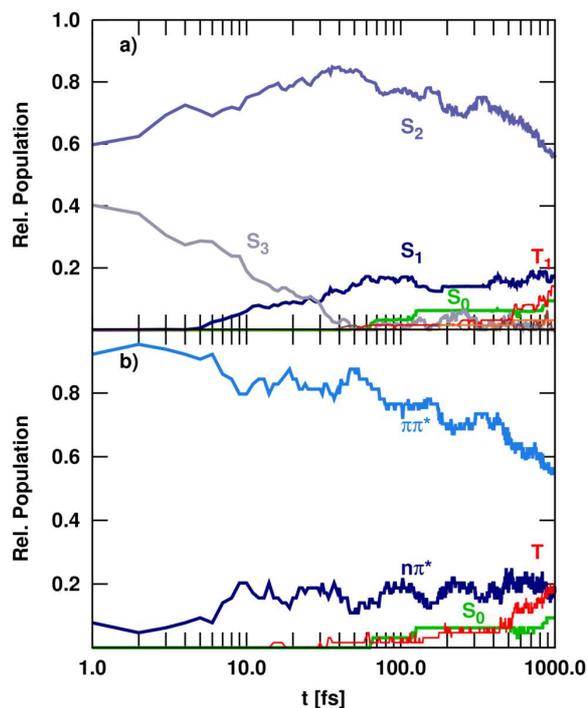
Fig. 8 Time evolution of the population of (a) electronic states and (b) spectroscopic states, including singlet and triplet states excited within the energy range to 6.59 ± 0.07 eV (Ensemble III).

For a more detailed comparison of the dynamical simulations with the experiment, it is useful to follow the time evolution not of the MCH states (S_0, S_1, etc) but of the spectroscopic states, i.e. the states classified according to their character ($n\pi^*$, $\pi\pi^*$, etc).[122] Indeed, time-dependent experiments do not monitor occupations in states ordered by energy, but follow the change of physical properties, such as oscillator strengths or ionization yields, that heavily depend on the character of the states. Therefore, we show the spectroscopic populations in Figure 6b for Ensemble II (the results for Ensemble III are qualitatively very similar). The comparison between both representations (panels a and b) shows a strong correlation of the S_2 state with the $\pi\pi^*$ character and the S_1 with $n\pi^*$. Initially, all trajectories start in a bright $\pi\pi^*$ state that corresponds to S_2 and S_3, recall Figure 3a. The decay of the S_3 population to the S_2 in the MCH picture hence corresponds to vibrational relaxation in the bright $^1\pi\pi^*$ state. A sketch in Figure 7b illustrates this pathway, where the $^1\pi\pi^*$ state is indicated as solid, lightblue curve. Along this path, IC to the dark $n\pi^*$ state (indicated as solid, dark blue curve) can occur. This $^1n\pi^*$ state mostly corresponds to the S_1 state in the MCH representation. A branching can lead further to the ring-opening

discussed above (n($\sigma\pi$)π^*, solid yellow). More importantly, the nπ^* is the doorway for ISC to the triplet states. ISC then leads to the $^3\pi\pi^*$ state (dashed, light blue), where vibrational relaxation towards the $^3\pi\pi^*$ minimum takes place (implying an IC from T_2 to T_1 in the MCH picture).
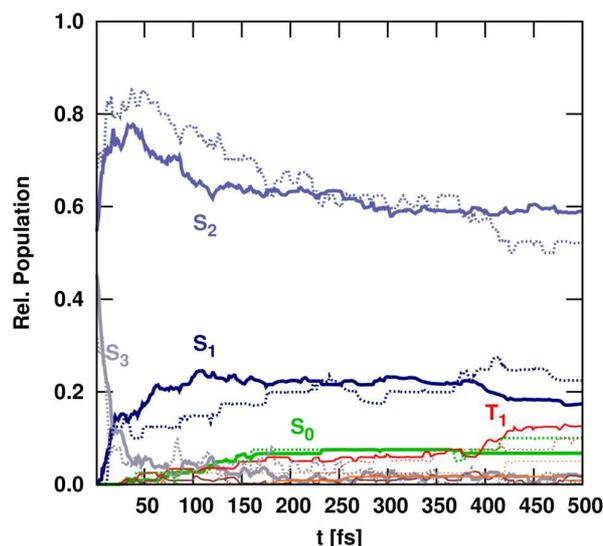
Fig. 9 Comparative time evolution of electronic state populations using the CASSCF(14,10) (Ensemble II, straight lines) and CASSCF(12,9) (Ensemble IV, dotted lines) level of theory.

As was shown before in Figure 3 and Table 1, a change of the active space of a CASSCF calculation leads to a change of the potential energy surfaces, which might lead to different dynamics. The impact of the active space onto the relaxation dynamics has been investigated with the dynamical simulations of Ensemble IV. Figure 9 shows an overlay of the electronic state populations of ensembles II (CASSCF(14,10)) and IV (CASSCF(12,9)) within the first 500 fs after δ-pulse excitation. Obviously, the initial populations mirror the Wigner distribution of geometries, so that Ensemble IV shows a higher population of S_2 in the first 200 fs. Also the initial relaxation from S_2 to S_1 is slower in Ensemble IV, as a result of the increased energy gap between those states at the CASSCF(12,9) level of theory in comparison to CASSCF(14,10) energies (see Table 1). After 200 fs, however, the differences between the electronic state populations are not substantial, suggesting that qualitatively the effect of the active space is not dramatic in this case. The differences in the approximate spectroscopic states (not shown) are even smaller, showing that the results are robust with respect to different active spaces with different state ordering at the Franck-Condon geometry (see Table 1).
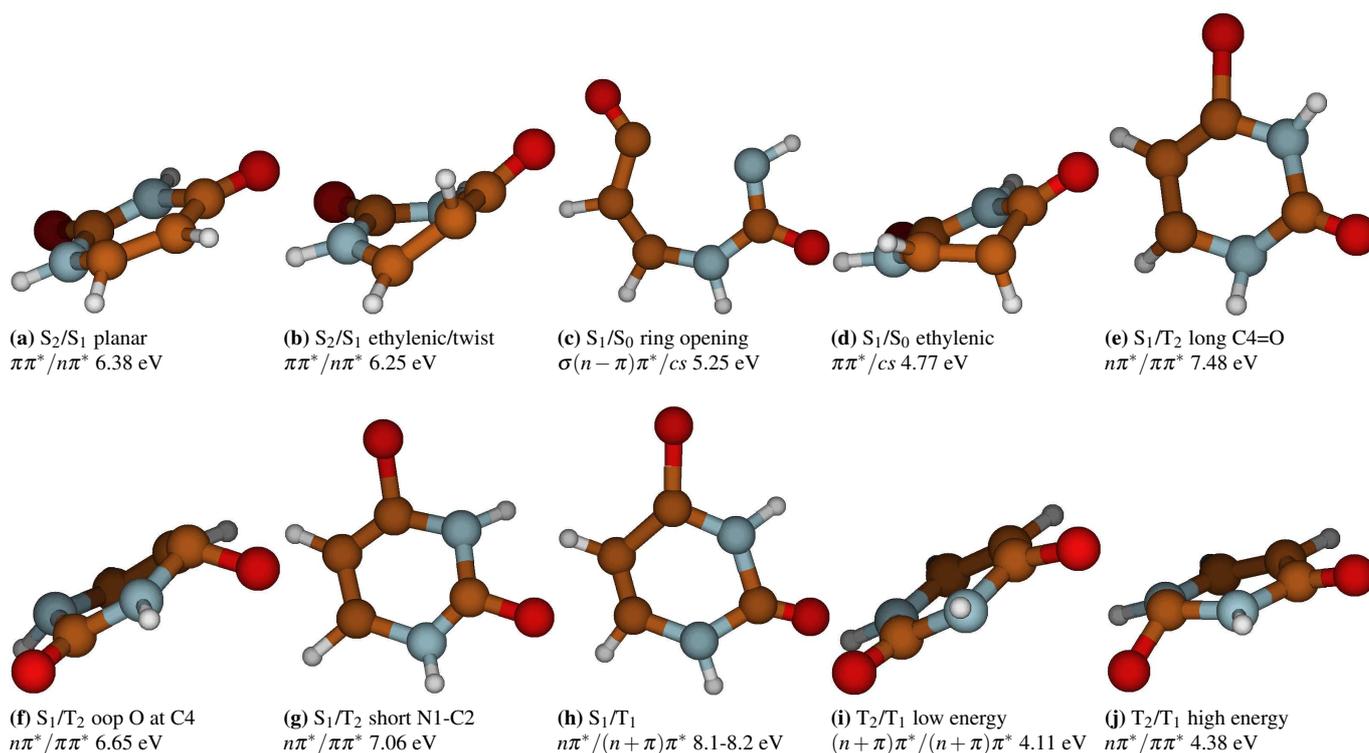
3.4 Conical Intersections and Hopping Structures

It is well-known that the population transfer in molecular dynamics simulations does not exactly happen at the minimum energy points of the seams of CoIns.[134] One can, however, relate the hopping geometries with the CoIns that can be optimized by means of static quantum chemical calculations. To this aim, all the hopping geometries where IC between singlets and IC between triplets occurred have been used as a starting point of a state crossing optimization. Some of the obtained geometries correspond to previously reported geometries, others are new crossing points which have been discovered by the dynamics. Figure 10 collects all the geometries optimized in this work as well es exemplary geometries that illustrate frequently observed features of ISC transitions.

Figure 10a corresponds to a $\pi\pi^*/n\pi^*$ CoIn that allows for S_2/S_1 hops. This structure has been previously found by Merchan et al.[135] and Lan et al.[102] and predicted at 5.92 eV above the equilibrium ground state energy at CASSCF level of theory. In our calculations, this structure is higher in energy (6.38 eV) due to the larger number of averaged states. One hop from S_2 and S_1 was found mediated by a different structure, depicted in Figure 10b, which is characterized by a twist of the ethylenic HC-CH group and a strong out-of-plane distortion of the aromatic ring. As already stated by Lan et al.[102], this reduction of planarity lowers the energy, in this case by 0.13 eV (CASSCF). However, precisely due to the strong distortion it is unlikely for many trajectories to proceed to this specific region of the potential energy surface (as corroborated by the present simulations where only one hop was found facilitated by this structure).

In the deactivation from S_1 to S_0, two geometries have been located. The most frequently used by uracil is the ring opening CoIn depicted in Figure 10c, where the the aromatic ring of the system is opened to maintain the planarity. The second CoIn, shown in Figure 10d, involves a twist of the ethylenic bond and it is therefore often referred to as the ethylenic S_1/S_0 CoIn. This latter structure was observed only in 3 hopping events. Both CoIns have been also reported by Nachtigallova et al.[103]. Thus, it can be concluded that the deactivation to the ground state within the first 200 fs is mediated by the ring opening CoIn and later deactivation happens via the ethylenic CoIn. These two mechanisms contribute to explain the biexponential increase behaviour that can be observed when fitting the populations of the S_0 and T_1 (vide infra).

ISC is mainly mediated by $S_1 \rightarrow T_2$ transitions. Several structures could be obtained where these states come close in energy (< 1 meV). These structures are dominated by heavy changes of the C=O bond lengths (Figure 10e) or ring puckering (Figure 10f). Ring deformations, such as the reduction of the N1-C2 bond length to only 1.22 Å can also lead to degeneracy between both states (Figure 10g).

(a) S$_2$/S$_1$ planar
$\pi\pi^*/n\pi^*$ 6.38 eV

(b) S$_2$/S$_1$ ethylenic/twist
$\pi\pi^*/n\pi^*$ 6.25 eV

(c) S$_1$/S$_0$ ring opening
$\sigma(n-\pi)\pi^*/cs$ 5.25 eV

(d) S$_1$/S$_0$ ethylenic
$\pi\pi^*/cs$ 4.77 eV

(e) S$_1$/T$_2$ long C4=O
$n\pi^*/\pi\pi^*$ 7.48 eV

(f) S$_1$/T$_2$ oop O at C4
$n\pi^*/\pi\pi^*$ 6.65 eV

(g) S$_1$/T$_2$ short N1-C2
$n\pi^*/\pi\pi^*$ 7.06 eV

(h) S$_1$/T$_1$
$n\pi^*/(n+\pi)\pi^*$ 8.1-8.2 eV

(i) T$_2$/T$_1$ low energy
$(n+\pi)\pi^*/(n+\pi)\pi^*$ 4.11 eV

(j) T$_2$/T$_1$ high energy
$n\pi^*/\pi\pi^*$ 4.38 eV

Fig. 10 Exemplary structures mediating intersystem crossing and optimized structures that mediate internal conversion in uracil.

In contrast to the S$_1 \rightarrow$ T$_2$ transitions, S$_1 \rightarrow$ T$_1$ ISC occurs rarely and only one hopping structure has been found where both states are energetically close to each other ($\Delta E < 0.1$ eV). This structure, see Figure 10h, is characterized by a strongly elongated C4=O bond (1.70 Å) and a deformed aromatic ring with a short C5-C6 bond (1.27 Å) and a long C4-C5 bond (1.55 Å).

IC between the T$_2$ and T$_1$ states is facilitated by two different geometries that are about 4.11 and 4.38 eV above the ground state equilibrium energy at CASSCF level of theory. The geometry lower in energy shows an out-of-plane displacement of the oxygen at C4 by about 21°. The C4=O bond is elongated to about 1.37 Å, wheres the C2=O bond is shortened to 1.20 Å (Figure 10i). This structure is very similar to the one described by Climent et al. [29] using quantum chemical calculations. The other CoIn lies 0.3 eV higher and shows the oxygen at C2 sticking out of the ring plane by about 54° and the C2=O bond elongated to 1.41 Å (Figure 10j).

3.5 Decay Times

Uracil has been subject of a number of time-dependent experimental studies, whose reported time constants and experimental setups are collected in Table 3. The first pump-probe ex-

periments in gas phase in uracil were made by Kang *et al.* [16]. Using a pump pulse of 267 nm excitation and multi-photon (n×800 nm) ionization as a probe, a monoexponential decay of the ionization signal yield with a time constant of 2.4 ps was fitted. Using higher time resolution, later studies were able to find an additional ultrashort time constant between 50 and 130 fs. Interestingly, except for the time-resolved photoelectron spectra of Ullrich and coworkers, [15] recorded with a 250 nm excitation and a 200 nm probe pulse, who fitted a 3-exponential decay (< 50 fs, 530 fs, 2.4 ps), most experiments find a biexponenatial decay behaviour after photoexcitation. In 2005, Canuel et al. [14] observed a decay of the transient ionization signal with time constants of 130 fs and 1.1 ps and the fluorescence upconversion experiments of Gustavsson et al. [17,18] recorded an ultrafast decay of fluorescence in aqueous solution with a time constant of less than 100 fs. Recent experiments of Kotur et al. [12] and Matsika et al. [13] combine TOF-MS with strong field ionization (n×780 nm) to obtain insight into the differences between the dynamics of different uracil fragments and the parent ion. In all their studies, they report a biexponential decay with a short time constant of 70-90 fs and a long time constant in the picosecond region (2.2-3.2 ps).

The time constants reported in previous theoretical studies are also listed in Table 3. Curiously, most theoretical studies

Table 3 Decay times of uracil as measured by pump-probe experiments in gas phase or solution (denoted by [a]) or calculated theoretically using different methods, as indicated. The symbol X indicates that the relevant paper discusses that timescale without giving a quantitative time constant. Numbers in parentheses in the third block refer to Ensemble III (see text).

setup		τ_1 [fs]	τ_2 [fs]	τ_3 [ps]	reference
experiment					
λ_{pump} [nm]	λ_{probe} [nm]				
267	n×800	-	-	2.4	Kang et al.[16]
250	200	<50	530	2.4	Ullrich et al.[15]
267	2×400	130	-	1.1	Canuel et al.[14]
267	330[a]	96	-	-	Gustavsson et al.[17]
267	330[a]	<100	-	-	Gustavsson et al.[18]
262	n×780 nm	70	-	2.2	Kotur et al.[12] (parent ion)
262	n×780 nm	90	-	3.2	Kotur et al.[12] (69+ fragment)
262	n×780 nm	70	-	2.4	Matsika et al.[13] (parent ion)
262	n×780 nm	90	-	2.6	Matsika et al.[13] (69+ fragment)
theoretical method					
FMS:CASSCF(8,6)		X	-	-	Hudock et al.[99]
SH:CPMD/BLYP		-	551-608	-	Nieber et al.[100]
					Doltsinis et al.[101]
SH:OM2/MRCI		21	570	-	Lan et al.[102]
SH:CAS(10,8)		-	650-740	>1.5-1.8	Barbatti et al.[24]
					Nachtigallova et al.[103]
SH:CAS(14,10)		X	X		Fingerhut et al.[104]
SH:CAS(14,10)		-	516		Fingerhut et al.[105]
this work					
S_0+T_1		-	-	2.4 ± 0.1 (4.2 ± 0.1)	Ensemble II (III)
S_0+T_1		63 ± 7 (48 ± 11)	-	2.8 ± 0.1 (5.2 ± 0.1)	Ensemble II (III)
$\pi\pi^*$		30 ± 1 (8 ± 1)	-	3.2 ± 0.1 (2.6 ± 0.1)	Ensemble II (III)

[a] fluorescence upconversion in aqueous solution

have obtained mono- or biexponential decays, where the time constants have mostly been assigned to the intermediate transient observed by Ullrich et al.[15]. Early FMS investigations of uracil by Hudock et al.[99] at the SA-CASSCF(8,6) level of theory report only small yields for IC within the first 500 fs after starting in the bright S_2 state. They claimed the experimentally observed ultrafast time constant (τ_1 in Table 3) to be the result of the system's initial vibrational relaxation towards the S_2 minimum, hand-in-hand with a significant increase of the ionization potential. In contrast to this, the Car-Parrinello molecular dynamics studies of Nieber et al.[100] and Doltsinis et al.[101] employing the BLYP functional, observe a single time constant of 608 fs for the $S_1 \rightarrow S_0$ deactivation at 300 K that decreases to 551 fs at 0 K temperature. The semiempirical surface-hopping simulations of Lan et al.[102] describe a biexponential decay with time constants of 21 and 530 fs, attributing the fast component to the $S_2 \rightarrow S_1$ transitions and the slow component to the relaxation from S_1 to S_0. The ab initio surface-hopping simulations reported by Barbatti et al.[24] and Nachtigallova et al.[103] also find a biexponential decay. De-

pending on the initial energy of the trajectories, to match a 250 nm or 267 nm excitation, they arrive at time constants of 650 fs and > 1.5 ps or 740 fs and > 1.8 ps, respectively. The faster of the two time constants is attributed to a relaxation to the ground state by either $\pi\pi^*/S_0$ decay after being trapped in the $\pi\pi^*$ minimum or a decay via an opening of the aromatic ring, leading to a mixed $\sigma(n-\pi)\pi^*$ character of the excited state when the transition to the ground state occurs. The longer time constant is attributed to the trapping of the trajectories in the dark $n\pi^*$ state before they relax to the ground state. In the recent study of Fingerhut et al.[104], explicit lifetimes are not given, but a fast $S_2(\pi\pi^*) \rightarrow S_1(n\pi^*)$ decay is observed as well, leading to a population of more than 20% of the initially dark $S_1(n\pi^*)$ state after less than 100 fs. In this state, the trajectories get trapped before they slowly proceed towards the S_0 ground state. A second study of Fingerhut et al.[105] using a larger ensemble of trajectories allowed them to extract a time constant of 516 fs for the depopulation of the bright S_2 ($\pi\pi^*$) state.

The third block of Table 3 collects time scales fitted in this

work from Ensemble II, values from Ensemble III are given in parentheses. As a prerequisite for fitting time constants that are comparable to experimental results, the neutral states leading to the experimental signal need to be identified. In case of an ionization setup, states with an ionization potential larger than the multiphoton ionization energy (i.e. states of the neutral molecule much lower in energy than the ground state of the ion) are assumed as dark, while all other states exhibit different brightnesses. It is often assumed that only the S_0 ground state is dark in these studies and the decay constant fits are based on this state's population. However, it has been shown for cytosine, that additionally the lowest triplet state (T_1), may be dark for the probe pulses typically employed in the experiments.[36] Since cytosine and uracil are structurally very similar and the quantum yield of S_0 obtained in our simulations is low, fitting was performed over the sum of S_0 and T_1 population, analogously to cytosine. Note that fitting ought to be carried out in the spectroscopic representation, but in our case, the S_0 coincides with the spectroscopic closed-shell state. Moreover, triplets cannot be distinguished in our way of determining the spectroscopic states, but we should include only the lowest triplet state in the fit. Thus, it is justified exceptionally to perform this part of the analysis using the S_0 and T_1 population. Fitting of the S_0 and T_1 population of ensemble II with a bi-exponential function yields two time constants of 63 fs and 2.8 ps.

The fs time constant stems from an early relaxation of population to S_0 and T_1 via the ring-opening CoIn (see figure 10c). However, static calculations at higher level of theory predict a strong destabilization of the ring-opening CoIn[103] and this pathway might actually be blocked. Therefore, a monoexponential fit was performed in addition, which yields a lifetime of 2.4 ps in good agreement with the experimentally observed ps time constant. Note however that any time constants in the range of several picoseconds have to be taken with a grain of salt since the simulation time was restricted to 1 ps. Also, the errors given in Table 3 represent the asymptotic standard errors of the fitting procedure alone and do not take into account further errors introduced by other approximations included in the simulation. Therefore, they do not represent errors with respect to real, experimentally measurable decay times. The mechanism behind the ps time constant involves several processes. Population relaxes from the $\pi\pi^*$ to the $n\pi^*$ state via the CoIns shown in figures 10a and 10b. From the $n\pi^*$ state, ISC leads mostly to the triplet T_2 state of $\pi\pi^*$ character in this region (exemplary structures are shown in figures 10e, 10f, 10g and 10h) followed by ultrafast IC to the lowest triplet state T_1 ($\pi\pi^*$ in this region). Population in the $^1n\pi^*$ that does not deactivate via ISC, can reach the S_0 ground state via the CoIns shown in figures 10c and 10d. Since the monoexponential fit describes the population decay well, it can be followed that ISC and ground state relaxation occur on com-

parable timescales.

So far, only the decay to states that are assumed completely dark has been considered in the fitting procedure. However, the experimental signal may be also changed by transitions to states where the brightness is different from the state occupied before but non-zero. This is the case in uracil for the transition from the $\pi\pi^*$ to the $n\pi^*$ state.[136,137] The $\pi\pi^*$ state is quickly depopulated to during the first few fs and afterwards the decay slows down considerably. Consequently, the depopulation of the $\pi\pi^*$ state was fitted biexponentially, yielding a time constant of 30 fs for the initial $\pi\pi^*$ to $n\pi^*$ decay. This relaxation proceeds via the CoIns shown in figures 10a and 10b, as already discussed for the ps time constant. However, the pathway here is slightly different. Initially, population is excited to the $\pi\pi^*$ state in the Franck-Condon region. From there, the ensemble of trajectories moves almost coherently towards the potential minimum of the $^1\pi\pi^*$ state and a fraction relaxes via said CoIns to the $^1n\pi^*$. Especially the planar structure shown in figure 10a is similar to the equilibrium structure of ground state uracil and therefore easily accesible from the Franck-Condon region. This fast decay of the bright $^1\pi\pi^*$ state population is also in qualitative agreement with the fast decay of fluorescence in the experiments of Gustavsson et al. in solution.[17,18] The trajectories remaining in the $^1\pi\pi^*$ state proceed towards the $^1\pi\pi^*$ minimum and only at later times the trajectories can move back to the $^1\pi\pi^*/^1n\pi^*$ CoIns. Since this return requires then a motion up in potential energy, the process is slowed down, leading to time constant of 3.2 ps. This constant is very similar to the one for the decay to S_0 and T_1, but slightly slower. Hence, the $n\pi^*$ state is slower replenished than depopulated, leading to a slight decay of its population.

Restricting the excitation energy to a small window below the absorption maximum (Ensemble III) increases the lifetimes of the monoexponential fit of S_0 and T_1 population to 4.2 ps and for the biexponential fit to 48 fs and 5.2 ps in agreement with the results of Nachtigallova et al.[103] The biexponential decay of $^1\pi\pi^*$ population in Ensemble III yields time constants of 8 fs and 2.6 ps. The first constant is even faster than in Ensemble II and hence also below the time resolution of the discussed experimental studies. The second constant is shortened as well and is now faster than the $S_0 + T_1$ time constant in the ps regime. As a consequence, the population of the $n\pi^*$ state remains more or less constant after an initial steep rise. This behaviour is in line with a summation of the seemingly different time constants of 8 fs, 2.6 ps ($\pi\pi^*$ depopulation) and 4.2 ps ($S_0 + T_1$ population). Note however that a multitude of different processes underly the found time constants including electronic transitions through various CoIns, vibrational relaxation and ISC. To find the connection between experimental time constants and the underlying physical processes is hence extremely challenging without the help of theoretical predictions. For a detailed discussion of the fit-

ting functions used to obtain the presented time constants, the interested reader is referred to the ESI†.

Interestingly, we do not find the intermediate time constant that was reported experimentally only once in Ref. [15] and could not be reproduced in later experimental studies. Theoretical studies assign this time constant to different processes, ranging from the S_0 population obtained from DFT and CASSCF studies with small active spaces [24,100,101,103] to the depopulation of the bright $S_2/\pi\pi^*$ state obtained using CASSCF with larger active spaces [105]. Thus, the origin of this time constant remains unclear.

Generally, the existence of an ultrafast time constant below 100 fs and a long time constant of several ps is in agreement with recent experimental studies [12–14] (see table 3). The short time constant is somewhat smaller than experiments suggest, what could be a result of the limited experimental time resolution and the theoretically employed δ-pulse excitation. The long time constant however is in excellent agreement with experimental results, confirming the validity of our findings.

4 Conclusions

In summary, this study provides clear evidence that intersystem crossing should be considered in any time-dependent treatment of the relaxation processes in uracil. Whereas time-independent quantum chemical computations can provide important intermediate structures of the potential energy surfaces, like conical intersections, minima and transition states, time-dependent dynamical studies are mandatory to evaluate the impact of these structures on the actual relaxation mechanism. As shown in this study, the exclusion of possible interactions between states of different multiplicity can qualitatively change the photophysical picture of the processes taking place.

Our dynamical calculations including both non-adiabatic and spin-orbit couplings show that the deactivation mechanism of uracil after UV light irradiation is the result of several competing processes. After 1 ps a significant fraction of the population can be found in the S_2, which mainly corresponds to the $\pi\pi^*$ state. The relaxation process can be characterized by a biexponential decay. A fast component τ_1 (30 fs) is attributed to the change of state character from the initially excited $\pi\pi^*$. The slower constant τ_3 (2.4 ps) arises from intersystem crossing in direct competition to internal conversion. The S_1 state, which is of $n\pi^*$ character, was found to be the doorway to triplet states, since population is trapped there for a sufficiently long time to allow intersystem crossing. In contrast to previous studies [104,105], only a very small amount of population returns to the ground state within 1 ps because ground state relaxation is quenched by intersystem crossing. The ground state relaxation is mediated by the ethylenic CoIn and the ring-opening path previously observed by Nachtigallova *et al.* [103].

The direct comparison of the decay lifetimes to those experimentally detected yields very good agreement and therefore supports the conclusion, that intersystem crossing from the first excited singlet state is in direct concurrence to internal conversion towards the ground state of uracil. Solvent effects could affect the observed time scales and the relative quantum yields of the involved processes. Therefore, the particular influence of solvation on intersystem crossing should be investigated in the future.

5 Acknowledgments

References

1. Richa, R. Sinha and D.-P. Häder, in *Photoinduced Phenomena in Nucleic Acids*, Springer Berlin Heidelberg, 2014, (in press) DOI: 10.1007/128_2014_531.
2. T. Schultz, E. Samoylova, W. Radloff, I. V. Hertel, A. L. Sobolewski and W. Domcke, *Science*, 2004, **306**, 1765–1768.
3. A. Abo-Riziq, L. Grace, E. Nir, M. Kabeláč, P. Hobza and M. S. d. Vries, *P. Natl. Acad. Sci. USA*, 2005, **102**, 20–23.
4. C. E. Crespo-Hernández, B. Cohen and B. Kohler, *Nature*, 2005, **436**, 1141–1144.
5. *Radiation Induced Molecular Phenomena in Nucleic Acids*, ed. M. K. Shukla and J. Leszczynski, Springer, 2008.
6. B. McFarland, J. Farrell, S. Miyabe1, F. Tarantelli, A. Aguilar, N. Berrah, C. Bostedt, J. Bozek, P. Bucksbaum, J. Castagna, R. Coffee, J. Cryan, L. Fang, R. Feifel, K. Gaffney, J. Glownia, T. Martinez, M. Mucke, B. Murphy, A. Natan, T. Osipov, V. Petrović, S. Schorb, T. Schultz, L. Spector, M. Swiggers, I. Tenney, S. Wang, J. White, W. White and M. Gühr, *Nat. Commun.*, 2014, **5**, 4235.
7. C. E. Crespo-Hernández, B. Cohen, P. M. Hare and B. Kohler, *Chem. Rev.*, 2004, **104**, 1977–2020.
8. G. W. Doorley, D. A. McGovern, M. W. George, M. Towrie, A. W. Parker, J. M. Kelly and S. J. Quinn, *Angew. Chem. Int. Ed.*, 2009, **7**, 123–127.
9. J. Peon and A. H. Zewail, *Chem. Phys. Lett.*, 2001, **348**, 255–262.
10. I. Buchvarov, Q. Wang, M. Raytchev, A. Trifonov and T. Fiebig, *P. Natl. Acad. Sci. USA*, 2007, **104**, 4794–4797.
11. D. Markovitsi, A. Sharonov, D. Onidas and T. Gustavsson, *ChemPhysChem*, 2003, **4**, 303–305.
12. M. Kotur, T. C. Weinacht, C. Zhou and S. Matsika, *IEEE J. Sel. Top. Quant.*, 2012, **18**, 187–194.
13. S. Matsika, M. Spanner, M. Kotur and T. C. Weinacht, *J. Phys. Chem. A*, 2013, **117**, 12796–12801.
14. C. Canuel, M. Mons, F. Piuzzi, B. Tardivel, I. Dimicoli and M. Elhanine, *J. Chem. Phys.*, 2005, **122**, 074316.
15. S. Ullrich, T. Schultz, M. Z. Zgierski and A. Stolow, *Phys. Chem. Chem. Phys.*, 2004, **6**, 2796–2801.

16 H. Kang, K. T. Lee, B. Jung, Y. J. Ko and S. K. Kim, *J. Am. Chem. Soc.*, 2002, **124**, 12958–12959.

17 T. Gustavsson, A. Banyasz, E. Lazzarotto, D. Markovitsi, G. Scalmani, M. J. Frisch, V. Barone and R. Improta, *J. Am. Chem. Soc.*, 2006, **128**, 607–619.

18 T. Gustavsson, N. Sarkar, E. Lazzarotto, D. Markovitsi and R. Improta, *Chem. Phys. Lett.*, 2006, **429**, 551–557.

19 C. T. Middleton, K. de La Harpe, C. Su, Y. K. Law, C. E. Crespo-Hernández and B. Kohler, *Annu. Rev. Phys. Chem.*, 2009, **60**, 217–239.

20 G. M. Roberts and V. G. Stavros, *Chem. Sci.*, 2014, **5**, 1698–1722.

21 B. Kohler, *J. Phys. Chem. Lett.*, 2010, **1**, 2047–2053.

22 T. Gustavsson, R. Improta and D. Markovitsi, *J. Phys. Chem. Lett.*, 2010, **1**, 2025–2030.

23 A. Giussani, J. Segarra-Martí, D. Roca-Sanjuán and M. Merchán, in *Photoinduced Phenomena in Nucleic Acids*, Springer Berlin Heidelberg, 2013, (in press) DOI: 10.1007/128_2013_501.

24 M. Barbatti, A. J. A. Aquino, J. J. Szymczak, D. Nachtigallová, P. Hobza and H. Lischka, *P. Natl. Acad. Sci. USA*, 2010, **107**, 21453–21458.

25 K. Kleinermanns, D. Nachtigallová and M. S. de Vries, *Int. Rev. Phys. Chem.*, 2013, **32**, 308–342.

26 S. Mai, M. Richter, P. Marquetand and L. González, in *Photoinduced Phenomena in Nucleic Acids*, ed. M. Barbatti, A. C. Borin and S. Ullrich, Springer Berlin Heidelberg, 2014, (in press) DOI: 10.1007/128_2014_549.

27 M. Merchán, L. Serrano-Andrés, M. A. Robb and L. Blancafort, *J. Am. Chem. Soc.*, 2005, **127**, 1820–1825.

28 J. J. Serrano-Pérez, R. González-Luque, M. Merchán and L. Serrano-Andrés, *J. Phys. Chem. B*, 2007, **111**, 11880–11883.

29 T. Climent, R. González-Luque, M. Merchán and L. Serrano-Andrés, *Chem. Phys. Lett.*, 2007, **441**, 327–331.

30 R. González-Luque, T. Climent, I. González-Ramírez, M. Merchán and L. Serrano-Andrés, *J. Chem. Theory Comput.*, 2010, **6**, 2103–2114.

31 M. Etinski and C. M. Marian, *J. Phys. Chem. A*, 2009, **113**, 11809–11816.

32 M. Etinski, J. Tatchen and C. M. Marian, *J. Chem. Phys.*, 2011, **134**, 154105.

33 M. Etinski, *J. Serb. Chem. Soc.*, 2011, **76**, 1649–1660.

34 P. M. Hare, C. E. Crespo-Hernández and B. Kohler, *P. Natl. Acad. Sci. USA*, 2007, **104**, 435–440.

35 J. Cadet and P. Vigny, *Bioorganic Photochemistry*, 1990, **1**, 1–272.

36 S. Mai, P. Marquetand, M. Richter, J. González-Vázquez and L. González, *ChemPhysChem*, 2013, **14**, 2920–2931.

37 *Physical Chemistry*, ed. D. A. McQuarrie and J. D. Simon, University Science Books: South Orange, NJ, 1997.

38 M. Richter, P. Marquetand, J. González-Vázquez, I. Sola and L. González, *J. Phys. Chem. Lett.*, 2012, **3**, 3090–3095.

39 G. A. Amaral, A. Arregui, L. Rubio-Lago, J. D. Rodríguez and L. Bañares, *J. Chem. Phys.*, 2010, **133**, 064303.

40 D. S. N. Parker, R. S. Minns, T. J. Penfold, G. A. Worth and H. H. Fielding, *Chem. Phys. Lett.*, 2009, **469**, 43–47.

41 R. S. Minns, D. S. N. Parker, T. J. Penfold, G. A. Worth and H. H. Fielding, *Phys. Chem. Chem. Phys.*, 2010, **12**, 15607–15615.

42 J. J. Cavaleri, K. Prater and R. M. Bowman, *Chem. Phys. Lett.*, 1996, **259**, 495–502.

43 Y. Ohshima, T. Fujii, T. Fujita, D. Inaba and M. Baba, *J. Phys. Chem. A*, 2003, **107**, 8851–8855.

44 H. Satzger, B. Schmidt, C. Root, W. Zinth, B. Fierz, F. Krieger, T. Kiefhaber and P. Gilch, *J. Phys. Chem. A*, 2004, **108**, 10072–10079.

45 H. J. van Ramesdonk, B. H. Bakker, M. M. Groeneveld, J. W. Verhoeven, B. D. Allen, J. P. Rostron and A. Harriman, *J. Phys. Chem. A*, 2006, **110**, 13145–13150.

46 C. Reichardt, R. A. Vogt and C. E. Crespo-Hernández, *J. Chem. Phys.*, 2009, **131**, 224518.

47 C. Yang, H. Su, X. Sun and M. W. George, *J. Chem. Phys.*, 2012, **136**, 204507.

48 N. Tamai, T. Asahi and H. Masuhara, *Chem. Phys. Lett.*, 1992, **198**, 413–418.

49 T. J. A. Wolf, D. Voll, C. Barner-Kowollik and A.-N. Unterreiner, *Macromolecules*, 2012, **45**, 2257–2266.

50 C. Ma, Y. Du, W. M. Kwok and D. L. Phillips, *Chem. Eur. J.*, 2007, **13**, 2290–2305.

51 S. T. Park, J. S. Feenstra and A. H. Zewail, *J. Chem. Phys.*, 2006, **124**, 174707.

52 Q. Ou and J. E. Subotnik, *J. Phys. Chem. C*, 2013, **117**, 19839–19849.

53 O. Schalk, P. Lang, M. S. Schuurman, G. Wu, M. Bradler, E. Riedle and A. Stolow, *EPJ Web of Conferences*, 2013, **41**, 05029.

54 M. Huix-Rotllant, D. Siri and N. Ferré, *Phys. Chem. Chem. Phys.*, 2013, **15**, 19293–19300.

55 D. Shemesh, Z. Lan and R. B. Gerber, *J. Phys. Chem. A*, 2013, **117**, 11711–11724.

56 R. A. Vogt, C. Reichardt and C. E. Crespo-Hernández, *J. Phys. Chem. A*, 2013, **117**, 6580–6588.

57 R. Morales-Cueto, M. Esquivelzeta-Rabell, J. Saucedo-Zugazagoitia and J. Peon, *J. Phys. Chem. A*, 2007, **111**, 552–557.

58 J. S. Zugazagoitia, C. X. Almora-Díaz and J. Peon, *J. Phys. Chem. A*, 2008, **112**, 358–365.

59 J. S. Zugazagoitia, E. Collado-Fregoso, E. F. Plaza-Medina and J. Peon, *J. Phys. Chem. A*, 2009, **113**, 805–810.

60 R. López-Arteaga, A. B. Stephansen, C. A. Guarin, T. I. Sølling and J. Peon, *J. Phys. Chem. B*, 2013, **117**, 9947–9955.

61 E. F. Plaza-Medina, W. Rodríguez-Córdoba and J. Peon, *J. Phys. Chem. A*, 2011, **115**, 9782–9789.

62 O. F. Mohammed and E. Vauthey, *J. Phys. Chem. A*, 2008, **112**, 3823–3830.

63 E. Collodo-Fregoso, J. S. Zugazagoitia, E. F. Plaza-Medina and J. Peon, *J. Phys. Chem. A*, 2009, **113**, 13498–13508.

64 C. Reichardt, C. Guo and C. E. Crespo-Hernández, *J. Phys. Chem. B*, 2011, **115**, 3263–3270.

65 C. Reichardt and C. E. Crespo-Hernández, *J. Phys. Chem. Lett.*, 2010, **1**, 2239–2243.

66 C. Reichardt and C. E. Crespo-Hernández, *Chem. Commun.*, 2010, **46**, 5963–5965.

67 R. Ghosh and D. K. Palit, *J. Phys. Chem. A*, 2012, **116**, 1993–2005.

68 C. E. Crespo-Hernández, G. Burdzinski and R. Arce, *J. Phys. Chem. A*, 2008, **112**, 6313–6319.

69 M. Pollum and C. E. Crespo-Hernández, *J. Chem. Phys.*, 2014, **140**, 071101.

70 L. Martínez-Fernández, I. Corral, G. Grannuci and M. Persico, *Chem. Sci.*, 2014, **5**, 1336–1347.

71 L. Martínez-Fernández, L. González and I. Corral, *Chem. Commun.*, 2012, **48**, 2134.

72 G. Cui and W. Thiel, *J. Phys. Chem. Lett.*, 2014, **5**, 2682–2687.

73 J. P. Gobbo and A. C. Borin, *Comp. Theor. Chem.*, 2014, **1040-1041**, 195–201.

74 G. Cui and W.-H. Fang, *J. Chem. Phys.*, 2013, **138**, 044315.

75 W. J. Schreier, T. E. Schrader, F. O. Koller, P. Gilch, C. E. Crespo-Hernández, V. N. Swaminathan, T. Carell, W. Zinth and B. Kohler, *Science*, 2007, **315**, 625–629.

76 M. Barbatti, *ChemPhysChem*, 2014, early access: http://dx.doi.org/10.1002/cphc.201402302.

77 C. Daniel, M.-C. Heitz, J. Manz and C. Ribbing, *J. Chem. Phys.*, 1995, **102**, 905–912.

78 C. Daniel, R. de Vivie-Riedle, M.-C. Heitz, J. Manz and P. Saalfrank, *Int. J. Quant. Chem.*, 1996, **57**, 595–609.

79 M.-C. Heitz, K. Finger and C. Daniel, *Coord. Chem. Rev.*, 1995, **159**, 171–193.

80 N. B. Amor, D. Ambrosek, C. Daniel and R. Marquardt, *Chem. Phys.*, 2007, **338**, 81–89.

81 C. Daniel, D. Guillaumont, C. Ribbing and B. Minaev, *J. Phys. Chem. A*, 1999, **103**, 5766–5772.

82 I. Bruand-Cote and C. Daniel, *Chem. Eur. J.*, 2002, **8**, 1361–1371.

83 R. Heydová, E. Gindensperger, R. Romano, J. Sýkora, J. Antonín Vlček, S. Zális and C. Daniel, *J. Phys. Chem. A*, 2012, **116**, 11319–11329.

84 C. Gourlaouen and C. Daniel, *Dalton Trans.*, 2014, early access: http://dx.doi.org/10.1039/c4dt01822b.

85 H. Brahim and C. Daniel, *Comp. Theor. Chem.*, 2014, **1040-1041**, 219–229.

86 P. J. Costa, M. J. Calhorda, S. Villaume and C. Daniel, *New J. Chem.*, 2008, **32**, 1904–1909.

87 M. Kayanuma, C. Daniel, H. Köppel and E. Gindensperger, *Coord. Chem. Rev.*, 2011, **255**, 2693–2703.

88 M. Bargheer, M. Gühr, P. Dietrich and N. Schwentner, *Phys. Chem. Chem. Phys.*, 2002, **4**, 75–81.

89 M. V. Korolkov and J. Manz, *J. Chem. Phys.*, 2004, **120**, 11522–11531.

90 M. Korolkov and J. Manz, *Chem. Phys. Lett.*, 2004, **393**, 44–50.

91 A. Alekseyev, M. Korolkov, O. Kühn, J. Manz and M. Schröder, *J. Photochem. Photobiol. A*, 2006, **180**, 262–270.

92 B. Maiti, G. C. Schatz and G. Lendvay, *J. Phys. Chem. A*, 2004, **108**, 8772–8781.

93 A. Cohen and R. B. Gerber, *Chem. Phys. Lett*, 2007, **441**, 48–52.

94 C. Lévêque, R. Taïeb and H. Köppel, *J. Chem. Phys.*, 2014, **140**, 091101.

95 S. Mai, P. Marquetand and L. González, *J. Chem. Phys.*, 2014, **140**, 204302.

96 L. Favero, G. Grannuci and M. Persico, *Phys. Chem. Chem. Phys.*, 2013, **15**, 20651–20661.

97 I. Tavernelli, B. F. Curchod and U. Rothlisberger, *Chem. Phys.*, 2011, **391**, 101–109.

98 L. Freitag and L. González, *Inorg. Chem.*, 2014, **53**, 6415–6426.

99 H. R. Hudock, B. G. Levine, A. L. Thompson, H. Satzger, D. Townsend, N. Gador, S. Ullrich, A. Stolow, and T. J. Martínez, *J. Phys. Chem. A*, 2007, **111**, 8500–8508.

100 H. Nieber and N. L. Doltsinis, *Chem. Phys.*, 2008, **347**, 405–412.

101 N. L. Doltsinis, P. R. L. Markwick, H. Nieber and H. Langer, in *Radiation Induced Molecular Phenomena in Nucleic Acids*, ed. M. K. Shukla and J. Leszczynski, Springer, 2008, pp. 265–299.

102 Z. Lan, E. Fabiano and W. Thiel, *J. Phys. Chem. B*, 2009, **113**, 3548–3555.

103 D. Nachtigallova, A. J. A. Aquino, J. J. Szymczak, M. Barbatti, P. Hobza and H. Lischka, *J. Phys. Chem. A*, 2011, **115**, 5247–5255.

104 B. P. Fingerhut, K. E. Dorfman and S. Mukamel, *J. Phys. Chem. Lett.*, 2013, **4**, 1933–1942.

105 B. P. Fingerhut, K. E. Dorfman and S. Mukamel, *J. Chem. Theory Comput.*, 2014, **10**, 1172–1188.

106 M. Richter, P. Marquetand, J. González-Vázquez, I. Sola and L. González, *J. Chem. Theory Comput.*, 2011, **7**, 1253–1258.

107 J. C. Tully, *J. Chem. Phys.*, 1990, **93**, 1061–1071.

108 P. Marquetand, M. Richter, J. González-Vázquez, I. Sola and L. González, *Faraday Discuss.*, 2011, **153**, 261–273.

109 J. J. Bajo, J. González-Vázquez, I. Sola, J. Santamaria, M. Richter, P. Marquetand and L. González, *J. Phys. Chem. A*, 2012, **116**, 2800–2807.

110 *Ultrafast Phenomena in Molecular Sciences*, ed. R. de Nalda and L. B. ares, Springer International Publishing, 2014, vol. 107, pp. 145–170.

111 M. E. Corrales, V. Loriot, G. Balerdi, J. González-Vázquez, R. de Nalda, L. Bañares and A. H. Zewail, *Phys. Chem. Chem. Phys.*, 2014, **16**, 8812–8818.

112 L. Verlet, *Phys. Rev.*, 1968, **165**, 201–214.

113 L. Verlet, *Phys. Rev.*, 1967, **159**, 98–103.

114 G. Granucci and M. Persico, *J. Chem. Phys.*, 2007, **126**, 134114.

115 H.-J. Werner and P. J. Knowles, *J. Chem. Phys.*, 1985, **82**, 5053.

116 P. J. Knowles and H.-J. Werner, *Chem. Phys. Lett.*, 1985, **115**, 259–267.

117 S. Matsika, *J. Phys. Chem. A*, 2004, **108**, 7584–7590.

118 H.-J. Werner, *Mol. Phys.*, 1996, **89**, 645–661.

119 P. Celani and H.-J. Werner, *J. Chem. Phys.*, 2000, **112**, 5546.

120 H.-J. Werner, P. J. Knowles, G. Knizia, F. R. Manby, M. Schütz, P. Celani, T. Korona, R. Lindh, A. Mitrushenkov, G. Rauhut, K. R. Shamasundar, T. B. Adler, R. D. Amos, A. Bernhardsson, A. Berning, D. L. Cooper, M. J. O. Deegan, A. J. Dobbyn, F. Eckert, E. Goll, C. Hampel, A. Hesselmann, G. Hetzer, T. Hrenar, G. Jansen, C. Köppl, Y. Liu, A. W. Lloyd, R. A. Mata, A. J. May, S. J. McNicholas, W. Meyer, M. E. Mura, A. Nicklass, D. P. O'Neill, P. Palmieri, D. Peng, K. Pflüger, R. Pitzer, M. Reiher, T. Shiozaki, H. Stoll, A. J. Stone, R. Tarroni, T. Thorsteinsson and M. Wang, *MOLPRO, version 2012.1, a package of ab initio programs*, 2012, see https://www.molpro.net/.

121 J. González-Vázquez and L. González, *ChemPhysChem*, 2010, **11**, 3554.

122 A note on the nomenclature of excited states is in order here. In the discussion of spectroscopical experiments, electronic state are often labelled according to their character, e.g. $\pi\pi^*$, $n\pi^*$ or closed shell. Also, observable spectroscopic properties like transition dipole moments are closely correlated with the state character and we hence term this nomenclature and the corresponding representation 'spectrocopic'. In contrast, the outcome of theoretical chemistry is usually given in terms of the eigenfunctions of the non-relativistic electronic Hamiltonian (= molecular Coulomb Hamiltonian, MCH). Here, the electronic states of a given multiplicity are ordered and labelled with respect to their energy, e.g. S_0, S_1, ... (in case of singlets). States strictly ordered by energy can never cross and the corresponding representation is thus sometimes called 'adiabatic' (greek: not passing through). However, if more than one multiplicity of states is considered, the term 'adiabatic' is not appropiate anymore. In order to avoid this confusion, we employ the term 'MCH representation'. It is important not to confuse the different labels, since e.g. if relaxation pathways are discussed, the representation matters. Exemplarily, a pathway in terms of the spectrocopic representation may start in a $\pi\pi^*$ state and from there relax directly to the closed-shell state. The same pathway in the MCH representation could start in S_2, from there lead to S_1, and then relax to S_0. In this example, we are faced with the situation that the $\pi\pi^*$ state corresponds to the S_2 state at some geometries and to the S_1 state at others. Such considerations also play a role when establishing a model to fit decay time constants. However, a conversion between the different representations is not straightforward and great care needs to be taken in all photorelaxation studies, when comparing theory and experiment.

123 J. Rejnek, M. Hanus, M. Kabeláč, F. Ryjáček and P. Hobza, *Phys. Chem. Chem. Phys.*, 2005, **7**, 2006–2017.

124 L. B. Clark, G. G. Peschel and I. Tinoco, *J. Phys. Chem.*, 1965, **69**, 3615–3618.

125 M. Schreiber, M. R. Silva-Junior, S. P. A. Sauer and W. Thiel, *J. Chem. Phys.*, 2008, **128**, 134110.

126 E. Epifanovsky, K. Kowalski, P.-D. Fan, M. Valiev, S. Matsika, and A. I. Krylov, *J. Phys. Chem. A*, 2008, **112**, 9983–9992.

127 C. M. Marian, *WIREs Comput. Mol. Sci.*, 2012, **2**, 187–203.

128 N. M. Masaaki Fujii, Teruhiko Tamura and M. Ito, *Chem. Phys. Lett.*, 1986, **126**, 583–587.

129 J. Lorentzon, M. P. Fülscher and B. O. Roos, *J. Am. Chem. Soc.*, 1995, **117**, 9265–9273.

130 J. J. Szymczak, M. Barbatti, J. T. S. Hoo, J. A. Adkins, T. L. Windus, D. Nachtigallová and H. Lischka, *J. Phys. Chem. A*, 2009, **113**, 12686–12693.

131 L. Buschhaus, J. Rolf and K. Kleinermanns, *Phys. Chem. Chem. Phys.*, 2013, **15**, 18371–18377.

132 M. A. El-Sayed, *J. Chem. Phys.*, 1963, **38**, 2834–2838.

133 M. A. El-Sayed, *Acc. Chem. Res.*, 1968, **1**, 8–16.

134 B. G. Levine and T. J. Martínez, *Ann. Rev. Phys. Chem.*, 2007, **58**, 613–634.

135 M. Merchán, R. González-Luque, T. Climent, L. Serrano-Andrés, E. Rodríguez, M. Reguero and D. Peláez, *J. Phys. Chem. B*, 2006, **110**, 26471–26476.

136 M. Spanner, S. Patchkovskii, C. Zhou, S. Matsika, M. Kotur and T. C. Weinacht, *Phys. Rev. A*, 2012, **86**, 053406.

137 M. Kotur, C. Zhou, S. Matsika, S. Patchkovskii, M. Spanner and T. C. Weihnacht, *Phys. Rev. Lett.*, 2012, **109**, 203007.